

Effect of Ti and Cr on dispersion, structure and composition of oxide nano-particles in model ODS alloys

A.J. London^a, S. Santra^d, S. Amirthapandian^b, B.K. Panigrahi^b, R.M. Sarguna^b,
S. Balaji^b, R. Vijay^c, C.S. Sundar^b, S. Lozano-Perez^a, C.R.M. Grovenor^a

^a Department of Materials, University of Oxford, 16 Parks Road, OX1 3PH, UK

^b Materials Science Group, Indira Gandhi Centre for Atomic Research, Kalpakkam – 603102, India

^c International Advanced Research Centre for Power Metallurgy and New Materials (ARCI), Balapur, Hyderabad – 500005, India

^d Department of Physics, Indian Institute of Technology Kharagpur, India

Abstract

Three model ODS alloys (Fe-0.3Y₂O₃, Fe-0.2Ti-0.3Y₂O₃ and Fe-14Cr-0.2Ti-0.3Y₂O₃) were prepared by ball milling and then hot extrusion to study the effect of Ti and Cr on the size, distribution, crystal structure and composition of the nano-oxide particles. All alloys were characterized by high resolution transmission electron microscopy (HRTEM), atom probe tomography (APT) and synchrotron- X-ray diffraction (S-XRD) to determine the distribution, structure and composition of the oxide nanoparticles samples. The median particle size was 9.6 nm, 7.7 nm and 3.7 nm for the Fe-Y₂O₃, Fe-Ti-Y₂O₃ and Fe-Cr-Ti-Y₂O₃ alloys respectively, so the presence of Ti resulted in a significant reduction in oxide particle diameter and the addition of Cr gave a further reduction in size. In the Fe-0.3Y₂O₃ alloy, the particles are found to be bcc Y₂O₃, whereas in the other two alloys (Fe-Ti-0.3Y₂O₃ and Fe-Cr-Ti-Y₂O₃), the oxide particles were found to be structurally consistent with both orthorhombic Y₂TiO₅ and fcc Y₂Ti₂O₇. Detailed APT studies showed Cr shells around oxide particles of all sizes in the Fe-Cr-Ti-Y₂O₃ alloy, that a range of cluster compositions are present and the particle chemistry varies with cluster size. We show that the addition of Cr has a strong effect on both the size and stoichiometry of the particles.

<http://dx.doi.org/10.1016/j.actamat.2015.06.032>

Keywords: *Oxide dispersion strengthened alloys; ODS; nano-structured ferritic alloys (NFA); HRTEM; synchrotron X-ray diffraction; XRD; Atom Probe Tomography (APT);*

Email: Andrew.london@materials.ox.ac.uk (A.J. London)

1 Introduction

Oxide dispersion strengthened (ODS) steels have been identified as a promising candidate structural material for Generation IV and fusion reactors because of their superior high-temperature mechanical properties and improved radiation resistance compared to conventional ferritic/martensitic steels [1–3]. These properties are achieved by introducing stable oxide dispersoids into the ferritic matrix which act as pinning sites for dislocations, sinks for radiation-induced point defects and limit grain growth [4–8]. These alloys are typically synthesized by ball milling which fragments and refines the original powders and intimately mixes the components [9,10]. The mechanically alloyed powders are consolidated by hot extrusion [11] or hot-isostatic pressing [12], during which Y-Ti oxide nanoclusters form [4,13,14]. There have been many attempts to synthesize different compositions of ODS alloys, and an impressive stability of the oxide particles under irradiation has been reported by several groups [4,12–17].

In addition to this experimental data, there have been several reports on the results of theoretical calculations. For example, Murali et al. [18] examined the possible effects of Cr on the clustering behavior of Ti, Y and O in bcc Fe by *ab initio* calculations, suggesting that the Cr interacts only weakly with vacancies and shows repulsive interactions with Y and Ti [18]. The authors demonstrated a core/shell structure for these nanoclusters in which the core is enriched in Y, O, Ti while the shell is enriched in Cr.

The aim of the present work was to understand the role of the individual alloying elements of Ti and Cr in controlling the evolution of the oxide particle dispersion, and the effect of Cr on the crystal structure of the oxide particles. Three compositions (all in wt%) were chosen for detailed study; Fe-0.3 Y₂O₃, Fe-0.2Ti-0.3Y₂O₃ and Fe-14Cr-0.2Ti-0.3Y₂O₃. The Fe-0.3Y₂O₃ alloy was selected on the basis of previous work that suggested that the addition of ~ 0.35wt% Y₂O₃ gave excellent creep strength [19], and it is also a simple system in which to study the chemistry and structure of Y₂O₃ particles in the bcc Fe matrix. It is widely accepted that the presence of Ti makes the particle dispersion finer and leads to the formation of a dispersion of small Y-Ti-O clusters [20]. In addition, a measured increase in creep strength is attributed to the decrease in particle radius and inter-particle spacing with increasing Ti concentration [20]. So our second alloy system was chosen to be Fe-0.2Ti-0.3Y₂O₃. Cr plays a vital role as a bcc ferrite (matrix) stabilizer as well as adding good corrosion resistance, but only a limited amount of work has been performed to probe the role of Cr in affecting

the dispersion and crystal structure of the oxide particles. Therefore, Cr was added to the third alloy: Fe-14Cr-0.2Ti-0.3Y₂O₃. For the first time, these three model ODS alloys were characterized with three different techniques, high-resolution transmission electron microscopy (HRTEM), atom probe tomography (APT) and synchrotron- X-ray diffraction (S-XRD) to determine the structure and composition of the oxide nanoparticles. The principal findings of present work are that the Cr addition leads to a reduction in particle size, the formation of Cr-rich shells around oxide nanoparticles of all sizes but has no significant effect on the oxide crystallography.

2 Experimental methods

The three model ODS alloys were prepared by mechanical alloying and hot extrusion. High purity elemental powders of Fe, Ti, Cr, and Y₂O₃ were weighed and mixed to give alloy precursors with the desired compositions of Fe-0.3Y₂O₃, Fe-0.2Ti-0.3Y₂O₃ and Fe-14Cr-0.2Ti-0.3Y₂O₃. The Y₂O₃ powder (Alfa Aesar) had an average particle diameter of ~22 nm and the bcc crystal structure. The powders were mechanically alloyed by ball milling (Simolayer CM-08) in an argon atmosphere for four hours at 1000 rpm with a ball to powder ratio of 10:1. The Fe-0.3Y₂O₃ and Fe-0.2Ti-0.3Y₂O₃ mechanically alloyed powders were extruded at 1050 °C followed by annealing at 950 °C for two hours and then air cooling [21]. The mechanically alloyed Fe-14Cr-0.2Ti-0.3Y₂O₃ powder was extruded at 1150 °C and then quenched and tempered at 750 °C for two hours and air cooled [22]. Finally, consolidated model ODS rods of 12 mm diameter were prepared from all three alloy compositions. The measured O, C and N content, as measured by glow discharge mass spectrometry, are given in Table 1. These are in agreement with the measurements of composition made by atom probe.

Transmission electron microscopy (TEM) was used in order to observe the microstructure and dispersion of the oxide particles. For all the samples, 300 μm thick disks were sliced from the extruded rods, mechanically polished to a thickness of ~50 μm and 3 mm diameter disks punched out. These disks were then electropolished to perforation with a solution of ethanol, 2-butoxy ethanol and perchloric acid in 7:2:1 ratio at a temperature of -35 °C. The samples were characterized with a LIBRA 200FE (Carl Zeiss) high-resolution transmission electron microscope operated at 200 kV. The information limit of the microscope is 0.13 nm. The diameters of the particles were measured from bright-field images using ImageJ software [23]. Additional energy-filtered observations were made using a JEOL 2200MCO FEG TEM in the 10-80 eV energy-loss range, using a protocol detailed

Table 1: Measurements of the bulk oxygen, carbon and nitrogen content of the three alloys in weight percent (glow discharge mass spectrometry).

Alloy	O (wt%)	C (wt%)	N (wt%)
Fe-0.3Y ₂ O ₃	0.46 ± 0.02	0.03	0.019 ± 0.002
Fe-0.2Ti-0.3Y ₂ O ₃	0.47 ± 0.01	0.02	0.009 ± 0.001
Fe-14Cr-0.2Ti-0.3Y ₂ O ₃	0.38 ± 0.01	0.02	0.006 ± 0.001

elsewhere [24]. Foil thickness measurements were performed using the log-ratio method [25].

X-ray diffraction measurements were performed on the I-11 beam line [26] at the DIAMOND Synchrotron Light Source. The diffractometer consists of five identical nine-crystal multi-analyzing crystal arms deploying 45 crystals and detectors mounted on the 2θ -circle at 30° intervals, thus producing a high peak to background signal. The diffraction experiments were done using a wavelength of 0.827136 Å. The disk shaped ODS samples were loaded in alumina boats as sample holder.

For APT studies, mechanically cut 20×0.5×0.5 mm bars were electropolished by standard methods using 20% perchloric acid in acetic acid (5-14V) and then 2% perchloric acid in 2-butoxy ethanol (3-6V) to give sharp APT needle specimens with a tip radius of 50–100 nm [27]. TEM observations using a Philips CM20 TEM were made of the needles prior to analysis by APT. Atom probe analyses were performed at 50 K using a LEAP-3000X HR instrument. A 532 nm wavelength laser with a pulse width of 10 ps, repetition rate of 200 kHz, pulse energy of 0.3–0.4 nJ and spot size of less than 10 µm was used to promote field evaporation. Oxide clusters were identified in the data using the method of maximum separation distance of Y, YO and TiO ions. Ions within a maximum separation (D_{\max}) of each other are considered clustered [28]. Only clusters with a sufficient number of ions (N_{\min}) are considered to be evidence for the detection of an oxide nanoparticle. A D_{\max} of core ions of 0.7–1.1 nm was used with a N_{\min} value between 8–25 selected, by the method described in [29], for each individual data set. Artefacts from splitting and joining of clusters were reduced by an appropriate choice of the cluster selection parameters N_{\min} and D_{\max} . With increasing D_{\max} only a slight (<0.05) increase in oxygen fraction was observed in the Y:Ti:O ratio of the clusters. The radius of the clusters is determined by the core extent measured parallel to the analysis direction. The extent rather than radius of gyration was chosen to allow direct comparison between atom probe and TEM data. Cluster concentration line profiles were calculated in MATLAB for every individual cluster, with a length normalized to the cluster size. In this way, profiles of large and small clusters could be combined on the same plot. Compositional errors due to the overlap of ion peaks in the mass to

charge spectrum were reduced by a deconvolution of overlapping peaks [27] on a per-cluster basis [30].

3 Experimental results

3.1 Size Distribution

Figures 1(a, b, c) show typical EFTEM images of the Y-N_{2,3} edge from TEM samples of the three alloys, and Figure 1(d, e, f) show histograms of the nanoparticle sizes measured from a representative set of bright-field TEM images. The modal particle sizes are 7.9, 6.6 and 3.2 nm for the Fe-0.3Y₂O₃, Fe-0.2Ti-0.3Y₂O₃ and Fe-14Cr-0.2Ti-0.3Y₂O₃ alloys respectively (solid vertical lines in Figures 1(d-f)). The particle number density was estimated by TEM to be 10²¹ to 10²² m³ for all three alloys, increased with the addition of Ti and increased further with the addition of Cr. The same alloys were studied by APT, and the size distributions of the detected Y-Ti-O clusters for all three alloys are also shown in Fig. 1(e) and 1(f). The cluster number density measured by APT was 0.08±0.04, 1.1±0.7 and 2.6±2.1×10²³/m³ for Fe-0.3Y₂O₃, Fe-0.2Ti-0.3Y₂O₃ and Fe-14Cr-0.2Ti-0.3Y₂O₃, alloys respectively. There were too few particles (nine) measured in the Fe-Y₂O₃ alloy to form a histogram. There is excellent agreement between the sizes measured from the TEM observations and the APT data. However, the cluster number density in the APT data is approximately an order of magnitude higher for the Ti and Cr alloys. The higher number density observed by APT is due to the higher sensitivity of APT compared to TEM, especially to the smallest particles, and because some particles may appear invisible in some diffraction conditions in the TEM.

Figure 1(d-e) shows that the addition of Ti drastically reduces the particle diameter compared to the Fe-0.3Y₂O₃ alloy. It has been suggested that the presence of Ti during mechanical alloying promotes the decomposition of Y₂O₃ and encourages the nucleation of fine Y-Ti-O clusters [14] which is consistent our observation of the increased particle number density. The addition of Cr further reduces the modal particle diameter from 6.6 nm to 3.2 nm (TEM) and increases the particle number density. APT analysis of Fe-14Cr-0.2Ti-0.3Y₂O₃ also shows a reduction in particle diameter, from 4.8 to 3.6 nm compared to the Fe-Ti-Y alloy, as shown in the atom maps in Figure 2(a-c). We should note that the consolidation temperature of the Cr-containing alloy was 1150 °C while for the Fe-0.2Ti-0.3Y₂O₃ alloy a lower temperature of 1050 °C was used. Therefore, we might expect that

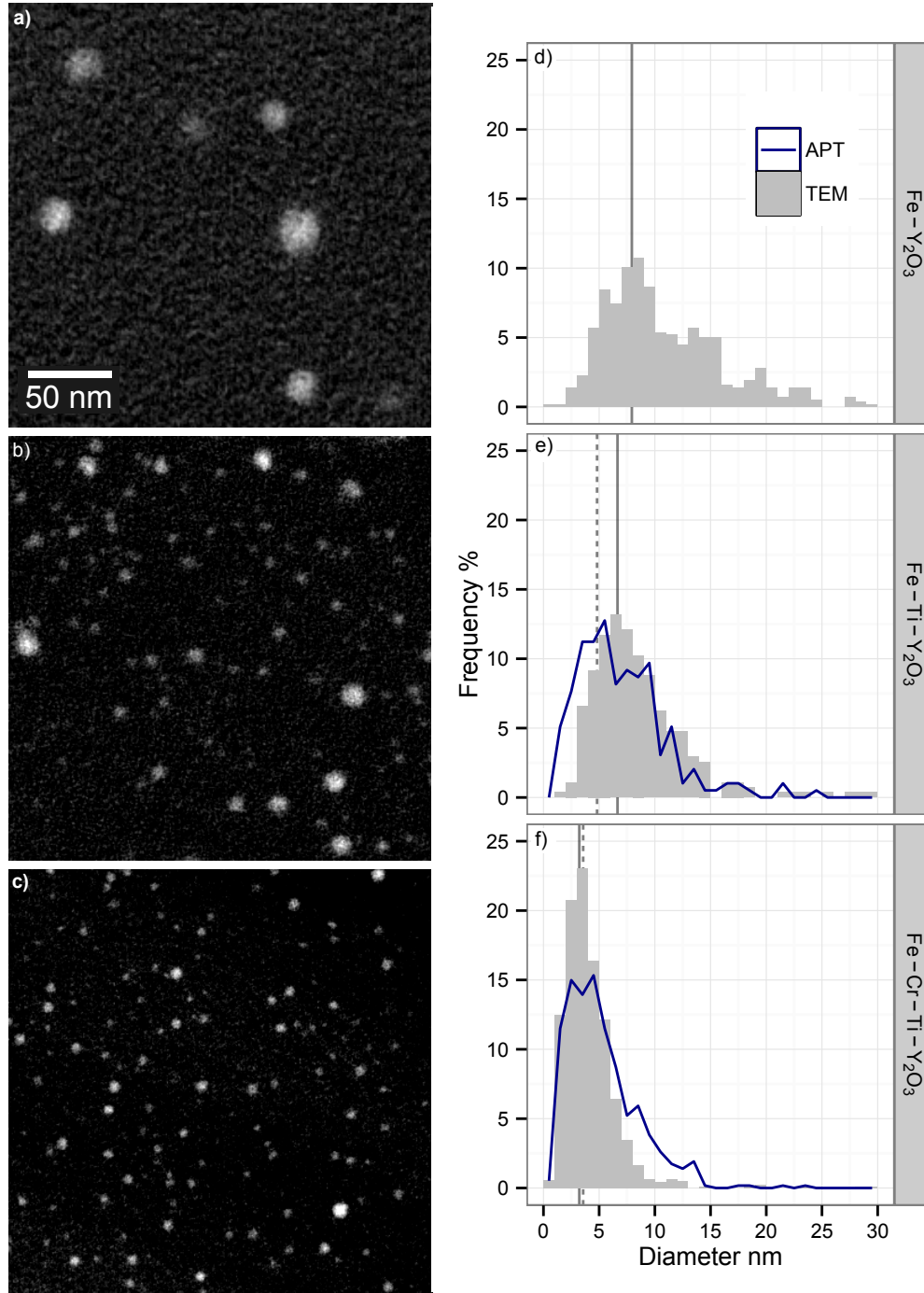


Figure 1: (a, b, c) EFTEM images of the Y-N_{2,3} edge in the alloys Fe-0.3Y₂O₃, Fe-0.2Ti-0.3Y₂O₃ and Fe-14Cr-0.2Ti-0.3Y₂O₃ respectively. The approximate foil thickness for each of the areas was estimated to be (a) 120, (b) 80 and (c) 40 nm. (d, e, f) show the particle size distributions for alloys Fe-0.3Y₂O₃, Fe-0.2Ti-0.3Y₂O₃ and Fe-14Cr-0.2Ti-0.3Y₂O₃ respectively as measured by TEM (solid bars) and APT (blue lines). Modal particle diameters: 7.9, 6.6 and 3.2 nm (median: 9.6, 7.7 and 3.7 nm) as measured by TEM are shown by solid vertical lines. The modal particle diameters as measured by APT are dashed vertical lines.

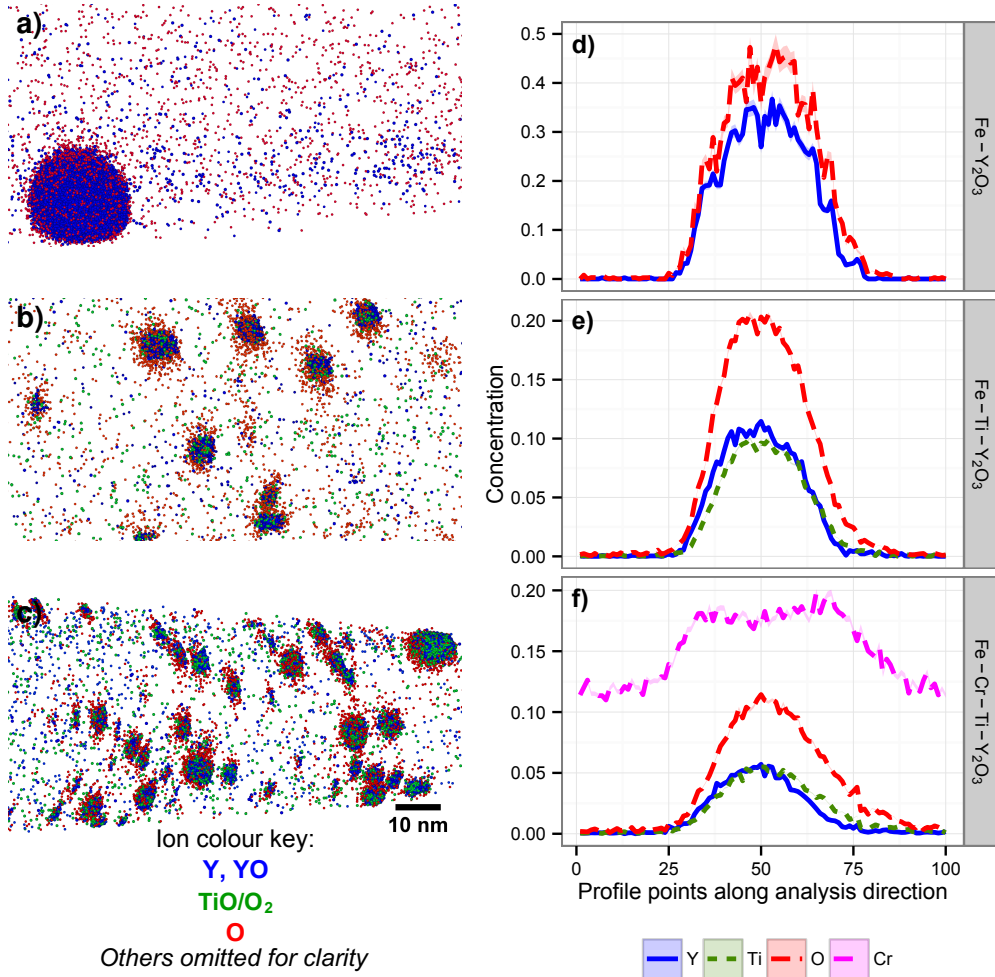


Figure 2: Example atom maps, reconstructed by APT, of the (a) Fe-0.3Y₂O₃, (b) Fe-0.2Ti-0.3Y₂O₃ and (c) Fe-14Cr-0.2Ti-0.3Y₂O₃ alloys. These images are the same scale with dimensions: 250 nm wide and 30 nm thick. The analysis direction is right to left. (d, e, f) Average composition line profiles along the analysis direction of clusters in the Fe-0.3Y₂O₃ (d), Fe-0.2Ti-0.3Y₂O₃ (e) and Fe - 14Cr-0.2Ti-0.3Y₂O₃ (f) alloys. The line profiles are for cluster diameters in the range: 0-28 nm, 4-12 nm and 2-8 nm for (d, e, f) respectively to correspond directly to the peak size range as measured by TEM. The length of these composition line profiles is normalised to the size of each cluster so that many line profiles can be averaged together, but the cross-sectional area of analysis was fixed at 1×1 nm for all the clusters.

the Cr-containing alloy should have a larger average particle size than the Fe-0.2Ti-0.3Y₂O₃ alloy based solely on the consolidation temperature [13]. Previous work on ODS alloys containing nine and 18 wt% Cr consolidated at the same temperature also show a reduced particle size in the higher Cr content alloy (2.5 nm compared to 4.5 nm modal particle size) [22].

3.2 Particle Chemistry (APT, TEM)

3.2.1 Average cluster chemistry

APT atom maps of the Y-, Ti- and O-containing ions are shown for the three different alloys in Figure 2(a-c). Most of the Ti and Y ions apparently identified outside of the clusters are due to noise in the

mass to charge spectrum; the combined Y and Ti content of the matrix was less than 0.05 at%. Some oxygen is detected in the matrix but could be due to oxygen present as a contaminant from the analysis chamber during the experiment as well as oxygen in solution in the ferritic matrix. Oxygen spreading is observed perpendicular to the analysis direction (Fig. 2(b)) as has been reported previously [31].

Figure 2(d-f), shows composition line profiles along the analysis direction of APT reconstructions through a representative set of oxide clusters for all three alloys. This is a convenient way to display the average chemistry of the nanoparticle in each alloy. The length of these composition line profiles is normalised to the size of each cluster so that many line profiles can be averaged together, but the cross-sectional area of analysis was fixed at 1×1 nm for all the clusters. In all the line profiles the balance is Fe which, in some cases has a concentration of >50 at% at the cluster centre. The apparent Fe content of the clusters increases with decreasing size but also with increasing acquisition voltage, as described elsewhere [30]. This is an artefact arising from the dissimilar evaporation fields of the oxide particles and the surrounding metal matrix, creating trajectory aberrations [32]. Anomalously high ionic densities are also detected at the core of the clusters [30] consistent with this explanation. These aberrations are greatest perpendicular to the analysis direction [33] and therefore their effect is minimized in the line profiles taken parallel to the APT analysis direction. In the larger clusters, no Fe is detected at their centre, and we conclude that the enhancement of Fe at the centre of the smaller clusters is certainly an artefact from the APT experiment.

The data in Figure 2(f) shows that Cr strongly segregates to the cluster surfaces with a local concentration of 20 at%. This behavior is consistent with observations of Cr-shells around clusters in ODS Eurofer alloys [31,32,34], but in the present study, by averaging many cluster profiles, the Cr-shell has been measured as a function of cluster size. The Cr-shell size scales linearly with cluster size, and was observed in average composition line profiles of clusters with a diameter as small as 4 nm that cannot be reliably analysed by TEM. Furthermore, the composition line profiles suggest that the Cr-shell is not oxidized. CrO molecular ions are detected, but not until the start of evaporation of the oxide particle core. The presence of a Cr-shell shows that Cr does not mix with the particles to influence their internal chemistry but segregates to their surface. The segregation of Cr to the surface of the nanoparticles is consistent with the results of theoretical calculations that indicate a repulsive interaction between Cr and Y/Ti [18]. The presence of Cr shell may also account for the observed reduction of particle size in the presence of Cr by reducing their coarsening rate at high temperature.

Figures 3(a) and 3(b) show the individual Y:Ti:O ratios of each oxide cluster detected by APT in the Fe-0.2Ti-0.3Y₂O₃ and Fe-14Cr-0.2Ti-0.3Y₂O₃ alloys. The points on the diagram are individual cluster compositions near the O-corner of the Gibbs ternary triangle for Y, Ti and O, with binary Y-oxide compositions along the bottom and binary Ti-oxide compositions along the left-hand edge. For comparison, the points marked 215 and 227 show the compositions of the two stable bulk oxides Y₂Ti₁₀O₅ and Y₂Ti₂O₇ respectively. These graphs do not include Fe or Cr, meaning that points of seemingly high oxygen content (to the left hand side of the ternary triangle) are actually Fe- or Cr-oxides. Only clusters with a diameter >6 nm are shown for clarity and for direct comparison with the other experimental techniques presented here. All the clusters have a similar O fraction of 0.60±0.03, but there is a statistically significant variation in the Y and Ti content over and above the statistical counting error associated with these APT measurements. This is a higher O-fraction than that measured in MA957 of 44 at% [35], which could be due to the per-cluster peak deconvolution methodology used in this work which gives a more reliable oxygen measurement by resolving mis-identified mass peaks [30]. The increased O-fraction measured here could also result from the relatively short milling time of 4 hours which may have left regions of high O-concentration. The clusters measured here are also of a much larger diameter than those reported in MA957; the sub 4 nm diameter clusters had an O-fraction closer to 55 at%.

The Y:Ti ratio of the larger clusters varies from 0.6-7.6, which again can only be explained by real variations in particle chemistry. Fig 3(c) and 3(d) show histograms of the Y/(Ti+O) ratios for the clusters in the Fe-0.2Ti-0.3Y₂O₃ and Fe-14Cr-0.2Ti-0.3Y₂O₃ alloys respectively. For Fe-14Cr-0.2Ti-0.3Y₂O₃ the peak of the distribution is at 0.22, consistent with the Y₂Ti₂O₇ composition, but there are shoulders on either side towards Ti-excess and Ti-deficient compositions compared to Y₂Ti₂O₇. Fig 3(c) shows a distribution of Y/(Ti+O) values of clusters in the Fe-0.2Ti-0.3Y₂O₃ alloy, with the peak between the two values consistent with the bulk Y₂Ti₁₀O₅ and Y₂Ti₂O₇ oxides. The actual variation in Y/(Ti+O) is 5%, compared to the counting error associated with the measurement of 0.5%.

Similar variations in particle composition greater than the statistical counting error have also been observed in other ODS alloys [32], and has been suggested that this is due to a change in composition with size [32,36]. The average Y:Ti ratios for clusters with diameters between 0-5, 5-7, 7-9, 9-11 and >11 nm are shown in Figure 4, to illustrate how the Y:Ti ratio changes systematically as a function of cluster diameter. The error bars indicate the variation in cluster compositions (upper and lower

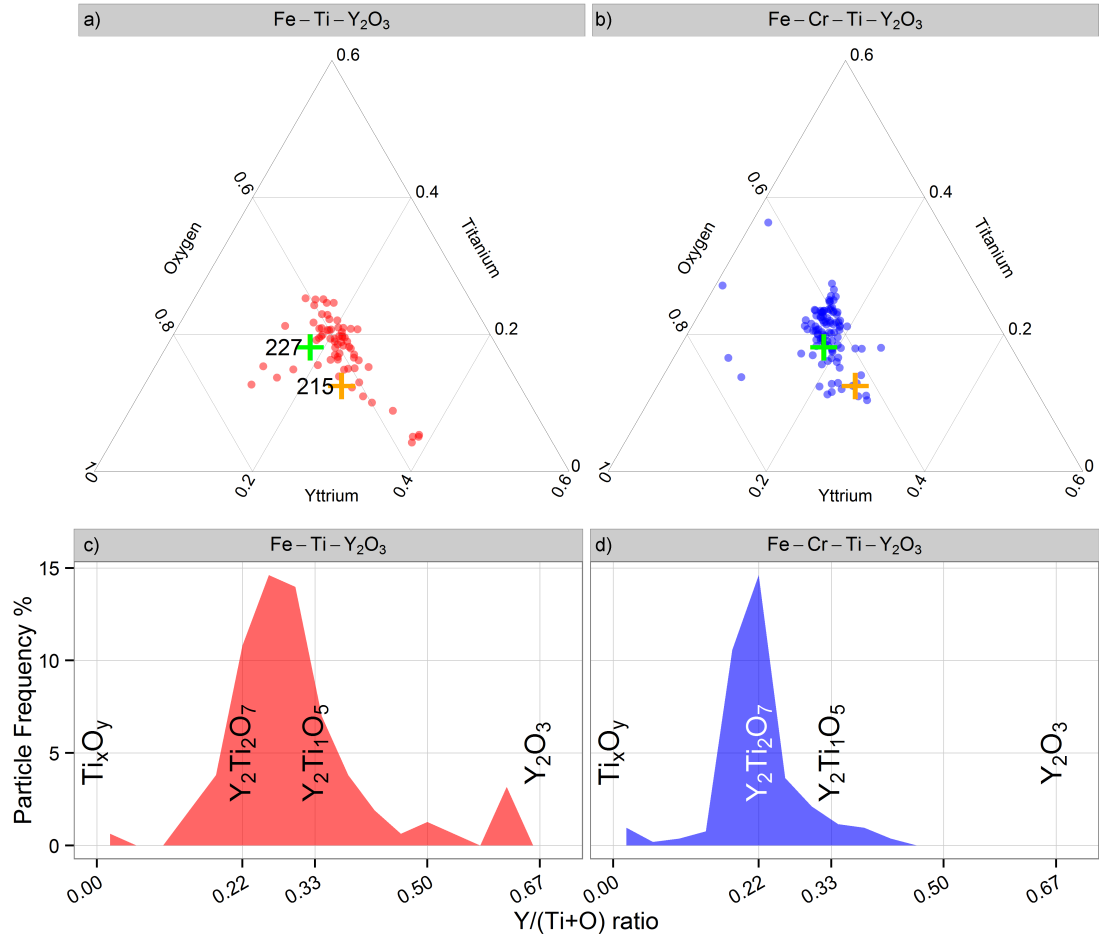


Figure 3: The O-corner of the Gibbs triangle showing the Y:Ti:O ratio of individual clusters in (a) the Fe-0.2Ti-0.3Y₂O₃ (left) and (b) Fe-14Cr-0.2Ti-0.3Y₂O₃ (right) alloys. Only the clusters with a diameter greater than 12 nm are shown for clarity. The positions of the stable Y₂TiO₅ and Y₂Ti₂O₇ oxide compositions are labeled as 215 (orange) and 227 (green) respectively. Histogram of the Y/(Ti+O) ratio of clusters in the (c) Fe-0.2Ti-0.3Y₂O₃ and (d) Fe-14Cr-0.2Ti-0.3Y₂O₃.

quartiles) not the error of the measurement.

3.2.2 Individual particle compositions.

Fe-0.3Y₂O₃ alloy The Y:O ratio measured by APT from 9 clusters in the Fe-0.3Y₂O₃ alloy was 0.665 ± 0.049 . Unlike the Y-oxides observed in other Ti-free alloys, such as EUROFER97 ODS [32], the clusters observed by APT in the alloys studied here were large (mean 18 nm in diameter) with a low number density $< 10^{20}/\text{m}^3$. This result shows that it is possible to reliably measure the correct stoichiometry of these Y-oxides by laser-assisted APT, at least when the cluster diameter is more than 8 nm, and that effects such as yttrium-loss due to multiple hits [37] or oxygen loss [38] are not significant in this case.

Fe-0.2Ti-0.3Y₂O₃ alloy APT analysis of the Fe-0.2Ti-0.3Y₂O₃ alloy resulted in the detection of 250 clusters in total. The average composition of these clusters, once isolated from the matrix, was Fe-4.0 Ti-4.2 Y-12.9 O (all ~2.0 at%). The large concentration of Fe apparently identified in the clusters is due to the trajectory aberrations mentioned above, which overlap the trajectories of evaporating matrix ions with those of the ions evaporating from the oxide clusters [32]. This is confirmed by the anomalously high ionic density recorded in the reconstructed data in the region of the oxide clusters of 100 ions/nm³, compared to the average (more physically meaningful) value recorded from the matrix of 30 ions/nm³. Removing the Fe ions gives an average composition of 9% Y, 20% Ti and 65% O, or an average stoichiometry of Y_{2.1}Ti_{2.2}O_{6.7}, very similar to the bulk stoichiometry of the stable Y₂Ti₂O₇ phase with some oxygen deficiency.

It is clear that the addition of Ti dramatically alters the oxide chemistry, and that the Ti partitions strongly into the oxide clusters leaving < 0.05 at% in the Fe-matrix. The addition of Ti to the alloy increases the metal:oxygen (M:O) ratio in the clusters from 2:3 (0.66) in the Fe-Y₂O₃ alloy to closer to 0.70. We also observe that the M:O ratio increases with decreasing cluster size, and that as the cluster size increases from the smallest 12 atom clusters to > 8 nm diameter clusters the median Y:Ti ratio decreases from 1.6 to 1.1, as shown in Figure 4. Though the average Y:Ti ratio is 1.2, Figure 3(b) shows the wide range of Y:Ti ratios observed. Some sub-5 nm diameter clusters have a low metal:oxygen ratio, (even as low as 1:1 after removing the ions associated with the matrix). This is consistent with previous atom probe studies that found small Y-Ti-O clusters in similar alloys with a M:O ratio of roughly 1.0 [32,35].

Fe-14Cr-0.2Ti-0.3Y₂O₃ alloy APT analysis of the Fe-14Cr-0.2Ti-0.3Y₂O₃ alloy resulted in the detection of more than 500 clusters. The average composition of these clusters isolated from the matrix was Fe-14.4 Cr-4.1 Ti-2.3 Y-11.7 O (with ~2 at% standard deviation between data sets). Again Fe and some Cr are included in the region identified as the clusters because of trajectory aberrations. After removing Fe and a proportional amount of Cr (matrix correction [32]), the average composition of the clusters is 27% Cr, 17% Ti, 9% Y and 47% O or Y₁₃Ti₂₃O₆₅ without Cr, which is not consistent with the stoichiometry of any stable bulk oxide. However, looking at the individual cluster compositions in Figure 3, there is a statistically significant variation in the composition, showing that a simple average value cannot be used to describe the true distribution of particle compositions. For example, there is one large (>10 nm radius) Ti-oxide cluster in the data set which will severely skew the

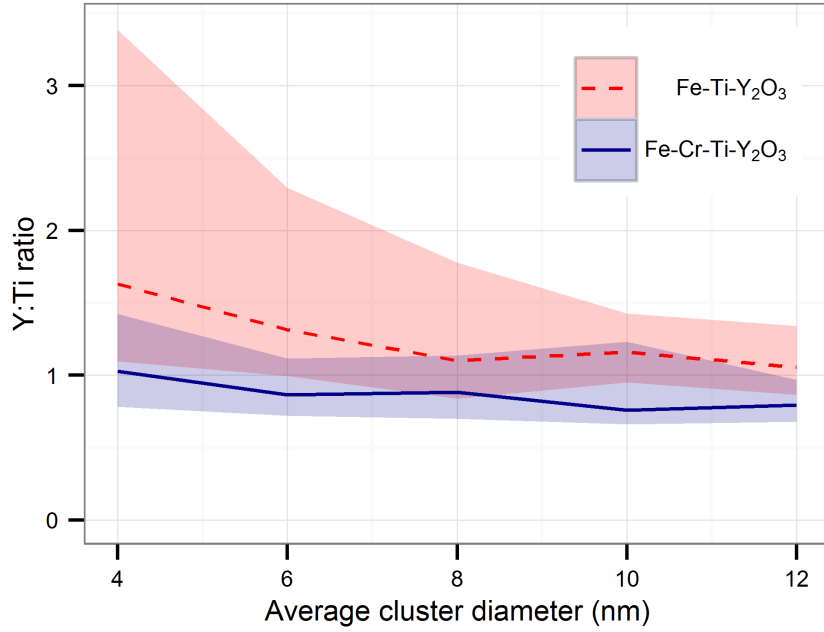


Figure 4: The median Y:Ti ratios of clusters in Fe-0.2Ti-0.3Y₂O₃ and Fe-14Cr-0.2Ti-0.3Y₂O₃ as a function of diameter. The shaded area indicates the upper and lower quartiles for each size range.

composition average. Cluster compositions vary systematically as a function of size, with the median Y:Ti ratio increasing with decreasing cluster size, from 0.8 (>4 nm) to 1.0. Figure 3(a) shows that the cluster Y:Ti:O ratios fall into three main groups, close to the stoichiometries of Y₂TiO₅, Y₂Ti₂O₇ and Y_{0.17}Ti_{0.22}O_{0.61} (Ti-excess compared to bulk compositions and more similar to YTi₂O₆). Some authors have suggested that the excess Ti measured may be due to segregation of Ti to the surface of the particles [39], but the compositional line profiles (figure 2(f)) show no evidence for segregation of Ti. Figure 3(c) shows quantitatively that the modal composition is similar to that of Y₂Ti₂O₇, but there are a number of clusters with Ti-excess and Ti-deficient compositions.

Non-stoichiometric particle compositions have been reported by APT [31,40,41] and there is some experimental evidence that suggests that a high concentration of vacancies are present [42]. The oxygen deficiency could be an artefact of APT and is most likely dependent on the particle chemistry and acquisition parameters [38]. It should be noted that the anion-deficient phases of Y₂Ti₂O_{6.48} and Y₂Ti₂O_{5.91} can be produced by reducing the pyrochlore Y₂Ti₂O₇ [43] and so these structures could be stabilized by a low oxygen activity during consolidation.

3.3 Particle Structure (TEM, XRD)

In order to determine the crystal structure of the dispersed particles, high-resolution transmission electron microscopy lattice imaging was performed on selected particles. Because of the similarity in inter-planar d spacing values from the possible crystal structures of Y-Ti-O oxides, two different d spacing values (for two hkl planes) and the angle between these planes is required to confidently identify the crystal structure. The crystallographic information obtained from fast Fourier transforms (FFT) of the structure images of oxide particles and identification of the zone axis orientation was compared with structural data from several possible compounds. These included monoclinic and bcc Y_2O_3 or Fe_2O_3 in the Fe- Y_2O_3 alloy, adding TiO_2 , Y_2TiO_5 , $\text{Y}_2\text{Ti}_2\text{O}_7$ and YTiO_3 for the alloy with Ti, and for the Fe-14Cr-Ti- Y_2O_3 alloy Cr_2O_3 , Cr_2TiO_3 and Cr_2TiO_5 .

Fe-0.3Y₂O₃ Figure 5(a) shows a typical high-resolution image taken from a region of the Fe- Y_2O_3 alloy containing an embedded oxide particle with a diameter of ~14 nm. The insert shows FFT taken from the highlighted region over the particle. We can identify three different sets planes, and the angles between these planes were calculated using ImageJ software. Two of these d spacings were found to be 2.9 Å, consistent with the {222} planes of bcc yttria, and the third one was 2.7 Å, consistent with the {400} planes in the same structure as given in JCPDS file (41-1105). After indexing, the zone axis was found to be $\langle 011 \rangle_{\text{Y}_2\text{O}_3}$. Two more bcc particles could be identified, and one particle was indexed to have the monoclinic Y_2O_3 structure (see Table 2), but for six others we could not confidently distinguish between the bcc and monoclinic structures. Fig. 5(b) shows the synchrotron XRD data for this alloy, and some broad peaks can be identified from both bcc and monoclinic Y_2O_3 , in agreement with the TEM observations. The other peaks in the XRD plot arise from the Fe matrix and iron oxides due surface oxidation before the synchrotron experiments. Using APT, the average Y:O ratio of 0.665 ± 0.049 reported above is in good agreement with the expected stoichiometry from the bcc Y_2O_3 phase identified in the TEM. Unfortunately, due to the trajectory aberrations associated with the analysis of oxide particles in a metal matrix [41], crystal planes in the oxide particles could not be resolved in the APT data, so we were unable to confirm the crystallography of the particles by this technique.

Fe-0.2Ti-0.3Y₂O₃ In the Fe-Ti- Y_2O_3 alloy, high resolution images from particles of various diameters were taken from electron transparent areas. Figure 5(c) shows a typical high resolution image

from a region of the specimen which is crowded with oxide particles. The FFT power spectrum of the highlighted region inside a particle of diameter ~ 7 nm is also inset. Two sets of d-spacings at 3.0 Å and 3.1 Å are identified, corresponding well with the {230} and {111} planes of Y_2TiO_5 respectively. The measured angle between the planes is 64° , which is close to the appropriate inter-planar angle in Y_2TiO_5 calculated from the data in JCPDS file 40-0795 of 64.6° .

Out of a total number of 14 particles analyzed by TEM in this material, five were identified as orthorhombic Y_2TiO_5 and three were found to be $\text{Y}_2\text{Ti}_2\text{O}_7$ (see summary in Table 2), the other particles could not be confidently identified. Fig. 5(d) shows the synchrotron XRD 2-theta scan from the Fe-Ti- Y_2O_3 alloy. The reflection at 16.3° is consistent with the strongest reflection from fcc $\text{Y}_2\text{Ti}_2\text{O}_7$ and to the left of this peak a small shoulder appears which we believe is due to the reflections from planes in orthorhombic Y_2TiO_5 . The peaks at 18.9° and 26.9° are also consistent with the fcc $\text{Y}_2\text{Ti}_2\text{O}_7$ phase. Other peaks were identified from the Fe matrix, a Fe-carbide and the alumina holder. Thus, the structure of the particles as inferred from the bulk XRD measurement and the individual measurement from TEM are in agreement, although the relative fraction of nanoscale fcc and orthorhombic phases is difficult to determine because of limitations of each of the techniques.

Fe-14Cr-0.2Ti-0.3Y₂O₃ The HRTEM image of a typical oxide particle of diameter ~ 8 nm in the Fe-14Cr-Ti- Y_2O_3 alloy is shown in Fig. 5(e). The inset is the FFT power spectrum of the highlighted region, and one can see three different d spacing values of 2.9, 2.8 and 2.5 Å consistent with the $\{2\bar{2}2\}$, $\{22\bar{2}\}$ and $\{400\}$ planes of fcc $\text{Y}_2\text{Ti}_2\text{O}_7$ (JCPDS 42-0413). In total, 28 particles of sizes ranging from 4 nm to 17 nm were examined in this alloy, of which eleven could be confidentially identified as having the orthorhombic Y_2TiO_5 structure and two were found to be fcc $\text{Y}_2\text{Ti}_2\text{O}_7$ (summarised in Table 2).

Fig. 5(f) shows the synchrotron XRD profile for the Fe-14Cr-Ti- Y_2O_3 alloy, and peaks from both the fcc $\text{Y}_2\text{Ti}_2\text{O}_7$ and orthorhombic Y_2TiO_5 phases are marked. The close proximity in 2θ position of peaks from these 2 phases, and the considerable peak broadening resulting from diffraction from nanoscale phases makes it difficult to be confident in identifying the presence of both phases in the matrix, and it is thus hard to make a direct comparison with the TEM observations. Comparison with the S-XRD data from the Fe-Ti- Y_2O_3 alloy shows a similar fraction of $\text{Y}_2\text{Ti}_2\text{O}_7$ but the Cr containing alloy has a smaller fraction of Y_2TiO_5 . Apart from the peaks corresponding to the Fe matrix, $\text{Y}_2\text{Ti}_2\text{O}_7$, Y_2TiO_5 and sample holder, peaks from Cr_2O_3 are also present due to surface oxidation.

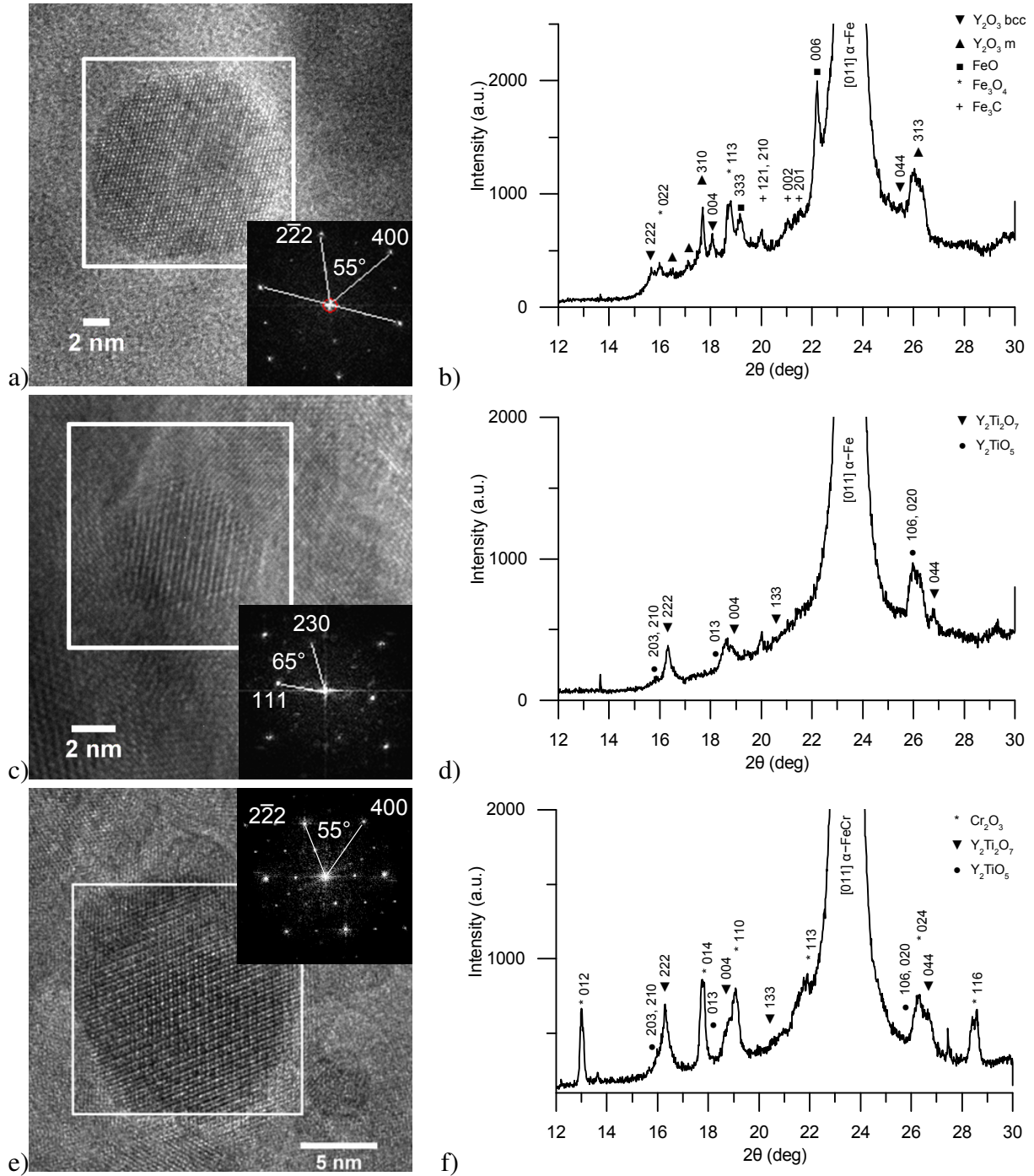


Figure 5: (a) HRTEM image from Fe-0.3Y₂O₃ with an embedded oxide particle; the FFT taken from the highlighted region is inset with various planes and angles indexed as bcc Y₂O₃, (b) X-ray diffraction intensity versus two theta angle obtained using synchrotron radiation for Fe-0.3Y₂O₃. (c) HRTEM image from Fe-0.2Ti-0.3Y₂O₃ with an embedded particle; the FFT taken from the highlighted region is inset and indexed as orthorhombic Y₂TiO₅, (d) X-ray diffraction intensity versus two theta angle obtained using synchrotron radiation on Fe-0.2Ti-0.3Y₂O₃. (e) HRTEM image from Fe-14Cr-0.2Ti-0.3Y₂O₃; the FFT taken from the highlighted region indexed as fcc Y₂Ti₂O₇. (f) X-ray diffraction intensity versus two theta angle obtained using synchrotron radiation on Fe-14Cr-0.2Ti-0.3Y₂O₃. The XRD peaks are labelled with their reflection and phase as given in the key. Peaks from the Al₂O₃ sample holder have not been indexed.

Table 2: Summary of HRTEM results from individual particles studied in the three ODS alloys including the size range of particles identified.

Alloy	Total number of particles analyzed	Phase			
		Y ₂ TiO ₅ (orthorhombic)	Y ₂ Ti ₂ O ₇ (fcc)	Y ₂ O ₃ (bcc)	Y ₂ O ₃ (monoclinic)
Fe-0.3Y ₂ O ₃	10	N.A	N.A	3 (10-20 nm)	1 (12 nm)
Fe-0.2Ti-0.3Y ₂ O ₃	14	5 (5-13 nm)	3 (6-10 nm)	0	0
Fe-14Cr-0.2Ti-0.3Y ₂ O ₃	28	11 (4-16 nm)	2 (5-15 nm)	0	0

3.4 Discussion

The TEM and APT data in Fig 1 are in excellent agreement, and show that the addition of Ti to the ferritic matrix significantly reduces the oxide particle diameter and the APT results show an increase in particle density by a factor of approximately 100. This is consistent with the previous suggestion [14] that the addition of Ti during mechanical alloying promotes the decomposition of Y₂O₃ which encourages the nucleation of Y-Ti-O complex oxide particles of finer size during any subsequent heat treatment. The enhanced thermal stability of the Y-Ti oxides over the Y-only oxides limits their growth, reducing the ultimate particle diameter after hot consolidation [44]. In our materials, the average particle size is slightly larger than reported for commercial alloys such as MA957 (2.4 nm diameter) [12], which could be due to the higher Ti content in the MA957 alloy or different milling conditions, in particular the shorter milling times.

Murali et al. [18] examined the possible effects of Cr on the clustering behavior of Ti, Y and O in bcc Fe by *ab initio* calculations. Their calculations suggest that the Cr interacts only weakly with vacancies and shows repulsive interactions with Y and Ti [18], and hence does not participate actively in the process of forming Y-Ti-O nanoclusters. This agrees with our observation that the addition of Cr only weakly affects the particle chemistry, without entering the particles, and binds strongly to the oxygen-rich surface of the oxide particles [45].

The frequency of particles with different crystal structures identified by TEM is shown in Table 2. In the HRTEM studies on the Fe-Y₂O₃ alloy, ten oxide particles were analyzed and only one, with a diameter of 12 nm, was found to be monoclinic yttria and the rest of them bcc Y₂O₃. Our starting powder was bcc Y₂O₃ and bulk yttria is most stable in the bcc phase up to 2598 K at atmospheric pressure [46–48], whereas nano-scale Y₂O₃ particles are stabilized in the monoclinic phase owing to the increasing importance of surface effects [19,46,49]. Chang et al. [50] also studied phase

transformations in nano-scale Y_2O_3 using electron microscopy and concluded that the critical grain size for the monoclinic to cubic transformation is in the range of 8-12 nm. It is thus not surprising that both our TEM and S-XRD data suggests the presence of both phases of Y_2O_3 . The results of the APT experiments confirm that the nanoparticles have compositions very close to that of bulk Y_2O_3 .

Our results from a careful study of the frequency of detecting orthorhombic Y_2TiO_5 or fcc $\text{Y}_2\text{Ti}_2\text{O}_7$ in the Fe-Ti- Y_2O_3 and Fe-14Cr-Ti- Y_2O_3 alloys are less consistent. The ground state formation energies of these phases have been evaluated to be -36.9 eV per formula unit of $\text{Y}_2\text{Ti}_2\text{O}_7$ (-3560 kJ mol⁻¹) and -27.7 eV per formula unit of Y_2TiO_5 (-2670 kJ mol⁻¹) respectively [51]. This suggests ultimately that the formation of $\text{Y}_2\text{Ti}_2\text{O}_7$ should be thermodynamically favoured over Y_2TiO_5 . However in the present study of the Fe-Ti- Y_2O_3 material, ~63% of the particles indexed by TEM were orthorhombic Y_2TiO_5 and this number increases to ~85% in the Fe-14Cr-Ti- Y_2O_3 alloy. This suggests that the presence of Cr favours the formation of the orthorhombic Y_2TiO_5 crystal structure as compared to fcc $\text{Y}_2\text{Ti}_2\text{O}_7$. However, in the Cr containing alloy the smaller average particle diameter makes the crystallographic identification more difficult which is reflected in the greater number of particles that could be indexed from the TEM data as either Y_2TiO_5 or $\text{Y}_2\text{Ti}_2\text{O}_7$ about 50% of all the particles imaged. The (203) and (210) Y_2TiO_5 reflections in synchrotron XRD data overlap with the strong (222) $\text{Y}_2\text{Ti}_2\text{O}_7$ reflection, but the Y_2TiO_5 reflections appear slightly stronger in the Fe-Ti- Y_2O_3 alloy. This may indicate an increased fraction of Y_2TiO_5 , or it could be an effect of the increased average particle diameter. The APT data from the Y_2TiO_5 and $\text{Y}_2\text{Ti}_2\text{O}_7$ alloy in Fig 3(b) shows some evidence of grouping of points around the 2 oxide phase stoichiometries, suggesting that the atom probe is able to distinguish between these two oxide phases. We detected in the Cr alloy many more individual clusters close to the $\text{Y}_2\text{Ti}_2\text{O}_7$ composition than around the Y_2TiO_5 point in the ternary triangle (emphasized in Fig 3d). Again this is not in agreement with the suggested shift from $\text{Y}_2\text{Ti}_2\text{O}_7$ to Y_2TiO_5 in the Cr alloy from the TEM data. We suggest that TEM results can discriminate between $\text{Y}_2\text{Ti}_2\text{O}_7$ or Y_2TiO_5 phases preferentially for larger particles and that the discrepancy with the S-XRD and APT data may lie in the difficulty of distinguishing the similar crystal structures in very small oxide particles. The S-XRD and APT results are in agreement with the relative formation energies of the bulk oxide phases.

The consistency of the characterization results must also be compared using the number of particles investigated, the intrinsic capability of the technique and the sensitivity of the measurements. We

have focused on using the particular strengths of the characterization techniques, TEM for the local structure, APT for the local chemistry and S-XRD for the bulk structure. We have used TEM to investigate the crystal structure only of the particles which could be confidently identified, leading to fewer than 100 analysed structures. The high number density of the clusters detected in APT gives over 1000 identified clusters in the data sets described above. S-XRD is a bulk measurement of cubic millimeters of material, meaning that some 10¹⁰ particles are in the integrated volume. But we must also consider the sensitivity of each of these techniques. Although S-XRD should be sensitive to volume fractions less than 1%, the experiment is complicated by the small size of the diffracting domains, <30 nm and could also be highly strained. There is also a difficulty in separating the characteristic cluster peaks from the much larger peaks from the ferrite matrix, and other phases like carbides and surface oxides, with only two positively identifiable peaks for the Y₂Ti₂O₇ and Y₂TiO₅ structures visible. The difference in number density observed with TEM and APT highlights the higher sensitivity of APT for small oxide clusters. In bright-field TEM there could be some ambiguity in distinguishing particles, and some may not be in a favorable orientation for diffraction, but the chemical sensitivity of APT means clusters have a high 'contrast' and it is even possible to distinguish between clusters of different compositions, Fig 3. The overall quality of the experimental data is improved by using as many techniques as possible and concentrating on the strengths of each.

From our APT data, the influence of adding Cr to the model is twofold; it affects the actual composition of the clusters as well as our ability to accurately measure that composition by atom probe analysis. The presence of Cr slightly increases the amount of oxygen measured by APT in the clusters (63% versus 60%), as seen by comparing the plots in Fig 3(a) and 3(b). We expect this result to be dependent on APT acquisition parameters, but this has not been investigated further here. The high affinity of Cr for oxygen may influence the evaporation process during the APT experiment, reducing the amount of oxygen lost during evaporation [38]. It also appears that without the Cr-addition there is a greater variation in the measured Y:Ti ratios, with some large clusters with a ternary fraction of 0.05 Ti and others with 0.25 Ti. The lower consolidation temperature of the Cr-free alloy (1050 °C rather than 1150 °C) could have prevented more thermodynamically stable oxide particle compositions forming.

The effect of Cr on the cluster-forming process has been less fully reported in the literature than the well known cluster-refining effect of Ti additions. For the smaller clusters in the Cr alloy, there is

in the APT data a large range of Y:Ti ratios from 1:2 to 1:0 (pure yttria). As noted by Sakasegawa et al, the apparent composition is dependent on the particle size [52], but unlike their findings our Y:Ti ratio increases for a significant proportion of the smaller clusters analysed rather than decreasing. Differences between the MA957 ODS alloy and the alloys examined here, such as impurity content [53] and the processing route, could explain these difference in the behavior of solute clustering at the atomic scale.

Without the addition of Cr, and in 9Cr ODS alloys, it is expected that the alloy would transform to austenite during the extrusion processes described above, although some residual ferrite may be retained [54]. Kim et al. observed an increased growth rate of the oxide particles which coincided with the transformation from alpha to gamma iron [55]. This could be explained both by the loss of coherency of the particles with the matrix and by the enhanced diffusion of the solute along gamma grain boundaries [56]. Therefore, the Cr addition may indirectly affect the particle growth rate by suppressing the alpha-gamma phase transformation of the matrix.

The presence of a Cr-rich shell in data like that shown in Figure 2, reveals that the Cr addition certainly interacts with the oxide particles, even when they are very small. Although the presence of a Cr-shell has been observed in individual clusters by TEM [34] and APT [31] this is the first systematic analysis that shows all sizes of clusters have a Cr-rich shell. The particle size distribution in the APT data in Figure 1 shows that despite the higher consolidation temperature the Cr-containing alloy still contains smaller oxide particles, suggesting that Cr acts to reduce the surface energy of the particles and so reduces the rate of coarsening or promotes nucleation of the clusters. The Cr around the periphery of the particles may also act to reduce strain and allow the particles to relax into structures more representative of the bulk oxides. This would explain why the compositions measured by APT split into two groups near the stable stoichiometries of the bulk $Y_2Ti_2O_7$ and Y_2TiO_5 oxides and why the clusters in the Fe-Ti- Y_2O_3 alloy have a wider spread of composition in Figure 3.

4 Conclusions

A major objective of the present work was to examine the role of individual alloying elements on the dispersion and crystal structure of oxide particles found in ODS alloys. Three model ODS alloys (Fe-0.3 Y_2O_3 , Fe-0.2Ti-0.3 Y_2O_3 and Fe-14Cr-0.2Ti-0.3 Y_2O_3) were prepared and characterized with transmission electron microscopy, APT and synchrotron XRD. We note that no one of these tech-

niques can give a complete picture of the nano-scale chemistry of these materials, but by combining HRTEM, APT and S-XRD results from the same materials we can be more confident that we can identify the key effects of adding Ti and Cr.

As is well known, the presence of Ti strongly effects the particle chemistry and reduces the average particle diameter. We have shown that the addition of Cr does not result in a dramatic change in particle chemistry but does refine the particle size distribution and segregates to all the particle/matrix interfaces. In the Fe-Y₂O₃ alloy predominately bcc Y₂O₃ particles were detected, but some monoclinic Y₂O₃ stabilized by size effects were also observed. In the other two alloys, our HRTEM analysis identifies both Y₂TiO₅ and Y₂Ti₂O₇ particles, and suggests that the addition of Cr makes the formation of the orthorhombic Y₂TiO₅ phase more likely. S-XRD also confirmed the presence of both of these oxide structures, but with a higher fraction of Y₂TiO₅ in the Fe-Ti-Y₂O₃ alloy. APT analysis of a large number of individual clusters shows a wide scatter in oxide composition centered around the stoichiometry of Y₂Ti₂O₇, and suggests a range of particle compositions are present in both the Cr-containing and the Cr-free alloy. Evidence of a Cr-rich shell around particles of all sizes is proposed to cause the reduction in particle size compared to the Cr-free alloy, and in addition the Cr may encourage stabilisation of the bulk alpha-ferrite phase during extrusion. Both these effects may play a very important role in improving the materials properties other than the corrosion resistance which is the primary aim of adding Cr to these alloys.

Acknowledgements

The authors acknowledge C.C.Tang for his valuable help in carrying out the synchrotron X-ray diffraction measurements at DIAMOND under the Indo-UK Collaborative programme funded by UK EPSRC Grant EP/I012400/1. AJL is supported by the Black Charitable Foundation.

References

- [1] S.-W. Kim, T. Shobu, S. Ohtsuka, T. Kaito, M. Inoue, M. Ohnuma, *Mater. Trans.* 50 (2009) 917, doi:10.2320/matertrans.MER2008439.
- [2] S. Ukai, T. Kaito, S. Ohtsuka, T. Narita, M. Fujiwara, T. Kobayashi, *ISIJ Int.* 43 (2003) 2038, doi:10.2355/isijinternational.43.2038.
- [3] S. Ukai, S. Mizuta, M. Fujiwara, T. Okuda, T. Kobayashi, *J. Nucl. Sci. Technol.* 39 (2002) 778,

doi:10.1080/18811248.2002.9715260.

- [4] G.R. Odette, M.J. Alinger, B.D. Wirth, *Annu. Rev. Mater. Res.* 38 (2008) 471, doi:10.1146/annurev.matsci.38.060407.130315.
- [5] L. Hsiung, M. Fluss, S. Tumey, J. Kuntz, B. El-Dasher, M. Wall, B. Choi, A. Kimura, F. Willaime, Y. Serruys, *J. Nucl. Mater.* 409 (2011) 72, doi:10.1016/j.jnucmat.2010.09.014.
- [6] J. Chen, P. Jung, W. Hoffelner, H. Ullmaier, *Acta Mater.* 56 (2008) 250, doi:10.1016/j.actamat.2007.09.016.
- [7] T. Hayashi, P.M. Sarosi, J.H. Schneibel, M.J. Mills, *Acta Mater.* 56 (2008) 1407, doi:10.1016/j.actamat.2007.11.038.
- [8] D. Haussler, M. Bartsch, U. Messerschmidt, B. Reppich, *Acta Mater.* 49 (2001) 3647, doi:10.1016/S1359-6454(01)00285-3.
- [9] Y. Kimura, S. Takaki, S. Suejima, R. Uemori, H. Tamehiro, *ISIJ Int.* 39 (1999) 176, doi:10.2355/isijinternational.39.176.
- [10] L. Dai, Y. Liu, Z. Dong, *Powder Technol.* 217 (2012) 281, doi:10.1016/j.powtec.2011.10.039.
- [11] A. Alamo, H. Regle, J.L. Bechade, *Adv. Powder Metall. Part. Mater.* 7 (1992) 169.
- [12] M.. Miller, D.. Hoelzer, E.. Kenik, K.. Russell, *J. Nucl. Mater.* 329-333 (2004) 338, doi:10.1016/j.jnucmat.2004.04.085.
- [13] M.J. Alinger, G.R. Odette, D.T. Hoelzer, *Acta Mater.* 57 (2009) 392, doi:10.1016/j.actamat.2008.09.025.
- [14] S. Ukai, S. Ohtsuka, *Energy Mater.* 2 (2007) 26, doi:10.1179/174892407X210357.
- [15] G.R. Odette, D.T. Hoelzer, *J. Miner. Met. Mater. Soc.* 62 (2010) 84, doi:10.1007/s11837-010-0144-1.
- [16] G.R. Odette, P. Miao, D.J. Edwards, T. Yamamoto, R.J. Kurtz, H. Tanigawa, *J. Nucl. Mater.* 417 (2011) 1001.
- [17] C. Robertson, B.K. Panigrahi, S. Balaji, S. Kataria, Y. Serruys, M.-H. Mathon, C.S. Sundar, *J. Nucl. Mater.* 426 (2012) 240, doi:10.1016/j.jnucmat.2012.04.001.
- [18] D. Murali, B.K. Panigrahi, M.C. Valsakumar, S. Chandra, C.S. Sundar, B. Raj, *J. Nucl. Mater.* 403 (2010) 113, doi:10.1016/j.jnucmat.2010.06.008.
- [19] G. Skandan, C.M. Foster, H. Frase, M.N. Ali, J.C. Parker, H. Hahn, *Nanostructured Mater.* 1 (1992) 313, doi:10.1016/0965-9773(92)90038-Y.
- [20] S. Ukai, M. Fujiwara, *J. Nucl. Mater.* 307-311 (2002) 749, doi:10.1016/S0022-3115(02)01043-7.
- [21] R. Vijay, M. Nagini, S.S. Sarma, M. Ramakrishna, A. V. Reddy, G. Sundararajan, *Metall. Mater. Trans. A* 45 (2013) 777, doi:10.1007/s11661-013-2019-x.
- [22] G. Sundararajan, R. Vijay, A. V Reddy, *Curr. Sci.* 105 (2013) 1100.
- [23] W. Rasband, ImageJ, [Http://imagej.nih.gov/ij/](http://imagej.nih.gov/ij/) (2014).

- [24] S. Lozano-Perez, V. de Castro Bernal, R.J. Nicholls, *Ultramicroscopy* 109 (2009) 1217, doi:10.1016/j.ultramic.2009.05.006.
- [25] T. Malis, S.C. Cheng, R.F. Egerton, *J. Electron Microsc. Tech.* 8 (1988) 193, doi:10.1002/jemt.1060080206.
- [26] S.P. Thompson, J.E. Parker, J. Potter, T.P. Hill, A. Birt, T.M. Cobb, F. Yuan, C.C. Tang, *Rev. Sci. Instrum.* 80 (2009) 075107, doi:10.1063/1.3167217.
- [27] M.K. Miller, A. Cerezo, M.G. Hetherington, G.D.W. Smith, *Atom Probe Field Ion Microscopy*, Oxford Science Publications, Oxford, 1996.
- [28] J.M. Hyde, C.A. English, in: *MRS 2000 Fall Meet. Symp.* Boston, MA, 2001, pp. 27–29.
- [29] C.A. Williams, D. Haley, E.A. Marquis, G.D.W. Smith, M.P. Moody, *Ultramicroscopy* 132 (2013) 271, doi:10.1016/j.ultramic.2012.12.011.
- [30] A. London, S. Lozano-Perez, M. Moody, S. Amirthapandian, B. Panigrahi, C. Sundar, C. Grovenor, *Ultramicroscopy* (2015), doi:10.1016/j.ultramic.2015.02.013.
- [31] E.A. Marquis, *Appl. Phys. Lett.* 93 (2008) 181904, doi:10.1063/1.3000965.
- [32] C.A. Williams, E.A. Marquis, A. Cerezo, G.D.W. Smith, *J. Nucl. Mater.* 400 (2010) 37, doi:10.1016/j.jnucmat.2010.02.007.
- [33] C. Oberdorfer, G. Schmitz, *Microsc. Microanal.* 17 (2011) 15, doi:10.1017/S1431927610093888.
- [34] M. Klimenkov, R. Lindau, A. Moslang, *J. Nucl. Mater.* 386–388 (2009) 553, doi:10.1016/j.jnucmat.2008.12.174.
- [35] M.K.K. Miller, K.F.F. Russell, D.T.T. Hoelzer, *J. Nucl. Mater.* 351 (2006) 261, doi:10.1016/j.jnucmat.2006.02.004.
- [36] H. Sakasegawa, L. Chaffron, F. Legendre, L. Boulanger, T. Cozzika, M. Brocq, Y. De Carlan, *J. Nucl. Mater.* 384 (2009) 115.
- [37] C.A. Williams, G.D.W. Smith, E.A. Marquis, *Ultramicroscopy* 125 (2013) 10, doi:10.1016/j.ultramic.2012.10.003.
- [38] A. Devaraj, R. Colby, W.P. Hess, D.E. Perea, S. Thevuthasan, *J. Phys. Chem. Lett.* 4 (2013) 993, doi:10.1021/jz400015h.
- [39] P. Wells, N. Cunningham, G.R. Odette, *Fusion Materials Semi-Annual Progress Report for the Period Ending December 31, 2011 DOE-ER-0313/51*, 2012.
- [40] D.J. Larson, P.J. Maziasz, I.S. Kim, K. Miyahara, *Scr. Mater.* 44 (2001) 359, doi:10.1016/S1359-6462(00)00593-5.
- [41] M.K. Miller, E.A. Kenik, K.F. Russell, L. Heatherly, D.T. Hoelzer, P.J. Maziasz, *Mater. Sci. Eng. A* 353 (2003) 140, doi:10.1016/S0921-5093(02)00680-9.

- [42] J. Xu, C.T. Liu, M.K. Miller, H. Chen, *Phys. Rev. B - Condens. Matter Mater. Phys.* 79 (2009), doi:10.1103/PhysRevB.79.020204.
- [43] M.A. Hayward, *Chem. Mater.* 17 (2005) 670, doi:10.1021/cm048220p.
- [44] M. Ratti, D. Leuvrey, M.H. Mathon, Y. de Carlan, *J. Nucl. Mater.* 386-388 (2009) 540, doi:10.1016/j.jnucmat.2008.12.1
- [45] A. Claisse, *Ab Initio Based Multi-Scale Simulations of Oxide Dispersion Strengthened Steels*, KTH, 2012.
- [46] V. De Castro, E.A. Marquis, S. Lozano-Perez, R. Pareja, M.L. Jenkins, *Acta Mater.* 59 (2011) 3927, doi:10.1016/j.actamat.2011.03.017.
- [47] T.B. Massalski, H. Okamoto, P.R. Subramanian, L. Kacprzak, others, *Binary Alloy Phase Diagrams*, ASM international, USA, 1990.
- [48] L. Pauling, M.D. Shappell, *Z. Krist.* 75 (1930) 128.
- [49] B. Guo, Z.-P. Luo, *J. Am. Ceram. Soc.* 91 (2008) 1653.
- [50] W. Chang, F. Cosandey, H. Hahn, *Nanostructured Mater.* 2 (1993) 29.
- [51] Y. Jiang, J.R. Smith, G. Robert Odette, *Acta Mater.* 58 (2010) 1536, doi:10.1016/j.actamat.2009.10.061.
- [52] H. Sakasegawa, F. Legendre, L. Boulanger, M. Brocq, L. Chaffron, T. Cozzika, J. Malaplate, J. Henry, Y. De Carlan, *J. Nucl. Mater.* 417 (2011) 229, doi:10.1016/j.jnucmat.2010.12.056.
- [53] K. Dawson, G.J. Tatlock, *J. Nucl. Mater.* 444 (2014) 252, doi:10.1016/j.jnucmat.2013.10.003.
- [54] M. Yamamoto, S. Ukai, S. Hayashi, T. Kaito, S. Ohtsuka, *Mater. Sci. Eng. A* 527 (2010) 4418, doi:http://dx.doi.org/10.1016/j.msea.2010.03.079.
- [55] S. Kim, S. Ohtsuka, T. Kaito, S. Yamashita, M. Inoue, T. Asayama, T. Shobu, *J. Nucl. Mater.* 417 (2011) 209, doi:http://dx.doi.org/10.1016/j.jnucmat.2011.01.063.
- [56] Y. Yazawa, T. Furuhashi, T. Maki, *Acta Mater.* 52 (2004) 3727.